Joint image segmentation and registration based on a dynamic level set approach using truncated hierarchical B-splines

Aishwarya Pawar [a], Yongjie Jessica Zhang [a,*], Cosmin Anitescu [b],
Timon Rabczuk [c]

[a] *Department of Mechanical Engineering, Carnegie Mellon University, USA*
[b] *Institute of Structural Mechanics, Bauhaus-Universität Weimar, Germany*
[c] *Department of Computer Engineering, College of Computer and Information Sciences, King Saud University, Riyadh, Saudi Arabia*

ARTICLE INFO

ABSTRACT

We present a novel approach for joint image segmentation and nonrigid registration using bidirectional composition based level set formulation. This efficient framework incorporates automatic structural analysis from image segmentation into the registration framework. This method has shown an improved performance as compared to carrying out segmentation and registration separately. Unlike previous approaches, the implicit level set function defining the segmentation contour and the spatial transformation function that maps the deformation for image registration are both defined using B-splines. This joint level set framework uses a variational form of an atlas-based segmentation together with large deformation based nonrigid registration. In addition, a bidirectional composition framework is introduced to incorporate a more symmetric update. The minimization of the variational form is accomplished by dynamic evaluations on a set of successively refined adaptive grids at multiple image resolutions. The improvement in the description of the segmentation result using higher order splines leads to a better accuracy of both the image segmentation and registration process. The performance of the proposed method is demonstrated on synthetic and medical images to show the improvement as compared to other registration methods.

© 2019 Elsevier Ltd. All rights reserved.

1. Introduction

Image registration is the process of finding accurate spatial correspondence between two or more images [1,2]. This field has several applications such as feature tracking [3] and fusion of images taken at different perspectives, time frames or even modalities [4]. Image segmentation is the process of delineating the shape of important features from images. The image is partitioned into multiple labeled regions denoting each object of interest [5]. This field incorporates shape information into the image analysis framework and is used for object recognition and classification of different regions of the image. Due to the large number of applications, both image segmentation and registration are important and challenging problems in image analysis.

Image registration can be classified into rigid and nonrigid registration based on the type of spatial mapping [6]. In rigid registration the image deformation is restricted to affine transformations such as translation, rotation, shearing and scaling. With nonrigid registration, more complex and localized deformations can be captured. However, the evaluation of

* Corresponding author.
E-mail address: jessicaz@andrew.cmu.edu (Y.J. Zhang).

an optimal smooth transformation in nonrigid registration is very difficult to attain [7]. Many registration algorithms have been proposed to achieve invertible and smooth transformation mappings, also known as diffeomorphisms. While many registration algorithms focus on achieving diffeomorphic transformations [8–14], it is still a very challenging problem. According to [15], the challenge in diffeomorphic transformation is how to evaluate a spatial mapping such that the composition of the forward and backward transformations is the identity transformation.

Image segmentation is a prolific research domain with a very large number of applications. In [16], an active contour model for segmentation was proposed based on the Mumford–Shah functional and level set method, which can carry out segmentation of complex structures in images. However, segmentation of noisy image data is a very challenging problem, particularly when working with images of poor resolution or when there are large inhomogeneities in the image intensities [17]. Thus, atlas-based segmentation methods were introduced in order to overcome the limitation of the segmentation algorithms. In these methods, the expertly segmented image known as the atlas, is used as the template image. Nonrigid deformation of the atlas is carried out to compute the segmentation of the target image which is generally noisy [18]. This problem is reduced to a registration algorithm and automatic segmentation of the target image is carried out even if the object boundaries are not very clear [19]. The unification of the atlas-based segmentation and registration methods in a joint framework is thus an interesting direction to pursue.

While image registration and segmentation are two different image analysis techniques that are performed for different applications, they pose several challenges when performed separately. Image registration can become challenging for large and complex image deformations. The minimization problem can become highly unconstrained and requires a considerable computational effort to achieve the optimal transformation. Thus several methods have been proposed to combine these two techniques to remove their respective drawbacks. Joint approaches have been shown to converge to better segmentation and registration results as compared to performing them separately [20,21]. Segmentation brings in structural information to give a good initial guess for the registration algorithm. The registration algorithm uses the object boundary information to accurately deform the features within the images. For the segmentation of noisy images, the atlas image which does not have any noise is first accurately segmented and deformed to align with the noisy target image. Thus, we obtain the segmentation result of the target image which is devoid of noise.

In this paper, an atlas-based joint segmentation and registration approach is proposed using truncated hierarchical B-splines (THB-splines). Here, the image is represented using B-spline based approximation method [22]. Through this approach, we can represent both the segmentation result and the evolving source image as a C^2 continuous object. The deformation field is represented using THB-splines to obtain more smooth and realistic deformations as compared to the finite difference method [20,21]. The main contributions of this paper are as follows:

- A joint variational level set framework based on THB-splines is proposed where image segmentation and registration are simultaneously carried out.
- Both the registered image and the level set function defining the segmentation contour are represented using C^2 continuous B-splines. The smooth description of the segmentation result using higher order splines improves the accuracy of the joint framework.
- The deformation fields are represented using higher order THB-splines. A bidirectional composition update for the deformation field is introduced to ensure smoothness and increased symmetry of the spatial mapping.

The paper is organized as follows: in Section 2, we introduce the joint image segmentation and registration framework. We apply the algorithm to 2D and 3D synthetic and medical image datasets in Section 3. Finally, concluding remarks and possibilities for future work are included in Section 4.

2. Mathematical model

In this section we discuss various components of the proposed joint segmentation and registration framework in detail. The smooth image representation using B-spline level set function is described in Section 2.1. The joint image segmentation and registration framework is described in Section 2.2 along with the proposed bidirectional compositional mapping. The description of adaptive local refinement using THB-splines and software implementation are provided in Sections 2.3 and 2.4, respectively.

2.1. Smooth representation of images

Computation of the image gradient is essential towards improving the accuracy of image processing algorithms. In [23], a C^2 smooth representation of grayscale images was proposed using a B-spline level set function. This was implemented in [14] for image registration to improve the numerical accuracy of gradient computation. In this paper, we represent registered and segmented images using the B-spline level set representation.

A grayscale image is a piecewise constant function that does not have a smooth representation of the object boundaries. Finite difference method cannot provide accurate gradient computation especially when the intensity changes abruptly or is subject to noise. A smooth representation of the image can improve the accuracy and convergence of the numerical

method through a more accurate computation of image gradients [14,22]. The B-spline level set function, $s(\mathbf{x})$, for the smooth reconstruction of the image is defined as

$$s(\mathbf{x}) = \sum_{k=1}^{n_3} \sum_{j=1}^{n_2} \sum_{i=1}^{n_1} a_{i,j,k} N_{i,j,k}^p(x, y, z), \tag{1}$$

where each level set coefficient $a_{i,j,k}$ is computed as

$$a_{i,j,k} = \frac{\int_\Omega N_{i,j,k}^p(x, y, z) g(x, y, z) \, d\Omega}{\int_\Omega N_{i,j,k}^p(x, y, z) \, d\Omega}. \tag{2}$$

Here $g(x, y, z)$ is the intensity value of the image and $N_{i,j,k}^p(x, y, z)$ represents a trivariate p^{th} order B-spline basis function evaluated at $\mathbf{x} = (x, y, z)$. Ω is the image domain and n_1, n_2 and n_3 denote the number of univariate basis functions in each direction. We define $R = \int_\Omega N_{i,j,k}^p(x, y, z) \, d\Omega$.

The computation of level set coefficients can be carried out efficiently using filtering methods [14]. A discrete B-spline kernel K is constructed using cardinal basis functions. In 1D, the cubic cardinal basis function $B^3(x)$ is defined as

$$B^3(x) = \begin{cases} \dfrac{(2+x)^3}{6}, & -2 \le x < -1, \\[2mm] \dfrac{2}{3} - x^2 - \dfrac{x^3}{2}, & -1 \le x < 0, \\[2mm] \dfrac{2}{3} - x^2 + \dfrac{x^3}{2}, & 0 \le x < 1, \\[2mm] \dfrac{(2-x)^3}{6}, & 1 \le x < 2, \\[2mm] 0, & \text{otherwise.} \end{cases} \tag{3}$$

The smooth representation of the grayscale image at the voxel center (x, y, z) can be written as

$$s(x, y, z) = \sum_{i=m_1}^{m_1+3} \sum_{j=m_2}^{m_2+3} \sum_{k=m_3}^{m_3+3} a_{i,j,k} B^3(x - i) B^3(y - j) B^3(z - k), \tag{4}$$

where $m_1 = \lceil x - 2 \rceil$, $m_2 = \lceil y - 2 \rceil$ and $m_3 = \lceil z - 2 \rceil$. The smooth representation can be easily evaluated as a convolution operation. The discrete cubic B-spline kernel K ($[4 \times 4 \times 4]$) is given as

$$K = \sum_{i=m_1}^{m_1+3} \sum_{j=m_2}^{m_2+3} \sum_{k=m_3}^{m_3+3} B^3(x - i) B^3(y - j) B^3(z - k). \tag{5}$$

Thus we can write the convolution as

$$s(x, y, z) = K \otimes a_{i,j,k}, \tag{6}$$

where $\otimes$ represents the convolution operator. Eq. (2) can be rewritten as

$$a_{i,j,k} = \frac{1}{R}(K \otimes M), \tag{7}$$

where the matrix M consists of grayscale intensity values in the integration domain. Details of how to evaluate M can be found in [14]. The B-spline kernel is of the same form as digital filters which are commonly used in image processing. The smooth representation removes irregularity of the image intensities and thus is an approximation to a Gaussian filter.

2.2. Joint level set and registration

We propose a variational formulation for the joint image segmentation and registration framework based on bidirectional composed updates. Given the source $I_s(\mathbf{x})$ and the target $I_t(\mathbf{x})$ images, the spatial transformation function $T(\mathbf{x})$ defines the optimum alignment between $I_s(\mathbf{x})$ and $I_t(\mathbf{x})$. In [23,24], the variational formulation for the active contour based segmentation is not solved using level set formulation [25], instead the segmented source image is deformed to align with the target image. In other words, an atlas-based segmentation model is used to evaluate the segmentation of the target image. From the source image, also known as the atlas, the level set contour $\phi(\mathbf{x})$ for the expertly segmented binary image is generated. Through the evaluation of the spatial transformation function $T(\mathbf{x})$, we compute $\phi(T(\mathbf{x}))$ and $I_s(T(\mathbf{x}))$ such that $I_s(T(\mathbf{x})) \approx I_t(\mathbf{x})$ and $\phi(T(\mathbf{x}))$ defines the level set contour for the segmented target image. To evaluate $T(\mathbf{x})$, we solve an optimization problem, which is given in a variational formulation. The minimization

of the energy functional is solved in iterative steps. At every time step, the spatial transformation function at the next time step $T(\mathbf{x})_{n+1}$ can be computed from the transformation function at the current time step $T(\mathbf{x})_n$ and the displacement field obtained in the next time step $\mathbf{V}_{n+1}$ in the following two ways:

- Additive update: $T(\mathbf{x})_{n+1} = T(\mathbf{x})_n + \mathbf{V}_{n+1}$;
- Composite update: $T(\mathbf{x})_{n+1} = T(\mathbf{x})_n \circ (\mathbf{x} + \mathbf{V}_{n+1})$.

The additive update is faster but cannot accurately represent large deformations. Composition updates can capture larger deformations which lead to faster convergence. However the computation of the composite update is more complex and time-consuming. In this paper, we follow the computation of the composition update using B-splines [14]. The transformation function at the next time step $T_{n+1}(\mathbf{x})$ is evaluated as

$$
\begin{aligned}
T_{n+1}(\mathbf{x}) &= T(\mathbf{x})_n \circ (\mathbf{x} + \mathbf{V}_{n+1}) \\
&= \sum_{i=m_1}^{m_1+3} \sum_{j=m_2}^{m_2+3} \sum_{k=m_3}^{m_3+3} \mathbf{A}_{i,j,k}^n N_{i,j,k}^p(\mathbf{x} + \mathbf{V}_{n+1}),
\end{aligned} \tag{8}
$$

where $\mathbf{A}_{i,j,k}^n = [a_{i,j,k}^{x,n}, a_{i,j,k}^{y,n}, a_{i,j,k}^{z,n}]$ are the B-spline level set coefficients updated at the current time step and $N_{i,j,k}^p(\mathbf{x} + \mathbf{V}_{n+1})$ are the B-spline basis functions evaluated at the displacement $(\mathbf{x} + \mathbf{V}_{n+1})$. To evaluate these coefficients, the discrete B-spline basis function kernel, K, is applied to the evaluated spatial transformation function $T_n(\mathbf{x})$. This results in a B-spline transformation function of the same order. Given $T_n(\mathbf{x}) = [T_n^x(\mathbf{x}), T_n^y(\mathbf{x}), T_n^z(\mathbf{x})]$, the level set coefficients are computed through convolution with the discrete B-spline basis kernel. Thus, we can write:

$$
\begin{aligned}
a_{i,j,k}^{x,n} &= \frac{1}{R}(K \otimes T_n^x(\mathbf{x})), \\
a_{i,j,k}^{y,n} &= \frac{1}{R}(K \otimes T_n^y(\mathbf{x})), \\
a_{i,j,k}^{z,n} &= \frac{1}{R}(K \otimes T_n^z(\mathbf{x})).
\end{aligned} \tag{9}
$$

We introduce a bidirectional mapping to increase the symmetry in image registration. In forward registration, the transformation function $f(\mathbf{x})$ is evaluated by morphing $I_s(\mathbf{x})$ to $I_t(\mathbf{x})$, whereas in backward registration, the spatial transformation function $b(\mathbf{x})$ is evaluated by morphing $I_t(\mathbf{x})$ to $I_s(\mathbf{x})$. At each iterative step, the control grid is initialized to identity transformation where the control points are set to Greville Abscissae in the image coordinate space [26]. The displacement field is evaluated by updating the position of control points at the particular iteration. In the bidirectional framework, the displacement fields in the forward ($V_f(\mathbf{x})$) and backward ($V_b(\mathbf{x})$) directions are defined as

$$
V_f(\mathbf{x}) = \sum_{m=1}^{N_b} \mathbf{C}_m^f B_m(\mathbf{x}) - \mathbf{x}, \tag{10}
$$

$$
V_b(\mathbf{x}) = \sum_{m=1}^{N_b} \mathbf{C}_m^b B_m(\mathbf{x}) - \mathbf{x}, \tag{11}
$$

where $\mathbf{C}_m^f$ and $\mathbf{C}_m^b$ are a set of control points associated with the trivariate basis functions $B_m(\mathbf{x})$. N_b represents the total number of basis functions with n_1, n_2 and n_3 as the number of basis functions in each parametric direction. $B_m(\mathbf{x})$ is the tensor product of pth order univariate B-spline basis functions $N_{i,p}(u)$, $N_{j,p}(v)$ and $N_{k,p}(w)$ defined on the open knot vectors $U = \{u_1, \ldots, u_{n_1+p+1}\}$, $V = \{v_1, \ldots, v_{n_2+p+1}\}$ and $W = \{w_1, \ldots, w_{n_3+p+1}\}$ spanning the image coordinate space in u, v and w directions, respectively. For 2D image registration, we use cubic B-splines to compute the displacement field ($p = 3$), whereas quadratic B-splines ($p = 2$) are used in 3D image registration. We use triquadratic basis functions for the 3D image registration to reduce the computational cost. The framework can be easily generalized to tricubic basis functions.

The energy functional for the joint framework is given as

$$
E(f(\mathbf{x}), b(\mathbf{x})) = E_{fid}(f(\mathbf{x}), b(\mathbf{x})) + E_{reg}(V_f(\mathbf{x}), V_b(\mathbf{x})), \tag{12}
$$

where $E_{fid}(f(\mathbf{x}), b(\mathbf{x}))$ is the fidelity term that carries out the joint segmentation and registration, and $E_{reg}(V_f(\mathbf{x}), V_b(\mathbf{x}))$ ~~regularizes the displace~~ment field. The energy functional is minimized in two steps [27]. We first minimize $E_{fid}(f(\mathbf{x}), b(\mathbf{x}))$ ~~to find new positions~~ of the control points $\mathbf{C}_m^f$ and $\mathbf{C}_m^b$. These control points are further optimized to $\mathbf{P}_m^f$ and $\mathbf{P}_m^b$ by ~~minimizing $E_{reg}(V_f(\mathbf{x}), V_b(\mathbf{x}))$.~~ The fidelity term is defined as

$$
\begin{aligned}
E_{fid}(f(\mathbf{x}), b(\mathbf{x})) &= \theta_1 \int_\Omega [(I_t(\mathbf{x}) - c_{in})^2 H_\epsilon(\tilde{\phi}(\mathbf{x})) + (I_t(\mathbf{x}) - c_{out})^2 (1 - H_\epsilon(\tilde{\phi}(\mathbf{x})))] d\Omega \\
&\quad + \theta_2 \int_\Omega [g^f(\mathbf{x})(\tilde{I}_s(\mathbf{x}) - I_t(\mathbf{x}))^2 + g^b(\mathbf{x})(\tilde{I}_t(\mathbf{x}) - I_s(\mathbf{x}))^2] d\Omega,
\end{aligned} \tag{13}
$$

where $\tilde{\phi}(\mathbf{x}) = \phi(f(\mathbf{x}))$, $\tilde{I}_s(\mathbf{x}) = I_s(f(\mathbf{x}))$ and $\tilde{I}_t(\mathbf{x}) = I_t(b(\mathbf{x}))$. The first term corresponding to θ_1 represents the binary segmentation of the target image by deforming the level set contour of the atlas image. $H_\epsilon(\mathbf{x})$ is the regularized Heaviside function and is defined as $H_\epsilon(\mathbf{x}) = \frac{1}{2}(1 + \frac{2}{\pi}\arctan(\frac{\mathbf{x}}{\epsilon}))$, where ϵ is the regularization parameter. c_{in} and c_{out} are the average intensities in the interior and exterior regions of the segmented target image and are defined as

$$c_{in} = \frac{\int_\Omega I_t(\mathbf{x})H_\epsilon(\tilde{\phi}(\mathbf{x}))\,d\Omega}{\int_\Omega H_\epsilon(\tilde{\phi}(\mathbf{x}))\,d\Omega}, \tag{14}$$

$$c_{out} = \frac{\int_\Omega I_t(\mathbf{x})(1 - H_\epsilon(\tilde{\phi}(\mathbf{x})))\,d\Omega}{\int_\Omega (1 - H_\epsilon(\tilde{\phi}(\mathbf{x})))\,d\Omega}, \tag{15}$$

respectively. The second term associated with θ_2 minimizes the sum of squared difference (SSD) in intensity values between the images. θ_1 and θ_2 are weighting parameters to balance segmentation and registration in the joint framework. The functions

$$g^f(\mathbf{x}) = \frac{1}{\sqrt{\gamma + (\frac{\partial \tilde{I}_s(\mathbf{x})}{\partial u})^2 + (\frac{\partial \tilde{I}_s(\mathbf{x})}{\partial v})^2 + (\frac{\partial \tilde{I}_s(\mathbf{x})}{\partial w})^2}} \tag{16}$$

and

$$g^b(\mathbf{x}) = \frac{1}{\sqrt{\gamma + (\frac{\partial \tilde{I}_t(\mathbf{x})}{\partial u})^2 + (\frac{\partial \tilde{I}_t(\mathbf{x})}{\partial v})^2 + (\frac{\partial \tilde{I}_t(\mathbf{x})}{\partial w})^2}} \tag{17}$$

are used to slow down the registration near the image boundaries while accelerating it in the homogeneous regions [28, 29], where γ is set to 10^{-12} to prevent division by zero. The energy functional is minimized using the L^2 gradient flow method with respect to the control points $\mathbf{C}^f(t)$ and $\mathbf{C}^b(t)$, where the variational formulation is converted to an ordinary differential equation. This is solved in a dynamic framework by updating the control point locations. We have

$$\frac{d\mathbf{C}_m^f(t)}{dt} = -\delta E_{m,fid}^f(f(\mathbf{x}), b(\mathbf{x})) \tag{18}$$

and

$$\frac{d\mathbf{C}_m^b(t)}{dt} = -\delta E_{m,fid}^b(f(\mathbf{x}), b(\mathbf{x})). \tag{19}$$

The first order variation of the energy function $E_{fid}(f(\mathbf{x}), b(\mathbf{x}))$ with respect to $\mathbf{C}_m^f(t)$ and $\mathbf{C}_m^b(t)$ is given as

$$\delta E_{m,fid}^f(f(\mathbf{x}), b(\mathbf{x})) = \theta_1 \int_\Omega [(I_t(\mathbf{x}) - c_{in})^2 - (I_t(\mathbf{x}) - c_{out})^2]H_\epsilon'(\tilde{\phi}(\mathbf{x}))\nabla\tilde{\phi}(\mathbf{x})B_m(\mathbf{x})\,d\Omega$$
$$+ 2\theta_2 \int_\Omega g^f(\mathbf{x})[\tilde{I}_s(\mathbf{x}) - I_t(\mathbf{x})]\nabla\tilde{I}_s(\mathbf{x})B_m(\mathbf{x})\,d\Omega, \tag{20}$$

$$\delta E_{m,fid}^b(f(\mathbf{x}), b(\mathbf{x})) = 2\theta_2 \int_\Omega g^b(\mathbf{x})[\tilde{I}_t(\mathbf{x}) - I_s(\mathbf{x})]\nabla\tilde{I}_t(\mathbf{x})B_m(\mathbf{x})d\Omega. \tag{21}$$

The control points are updated based on the dynamic scheme [29]:

$$\frac{\mathbf{C}_m^f - \mathbf{C}_{m,0}^f}{\epsilon_t} = -\delta E_{m,fid}^f(f(\mathbf{x}), b(\mathbf{x})), \tag{22}$$

$$\frac{\mathbf{C}_m^b - \mathbf{C}_{m,0}^b}{\epsilon_t} = -\delta E_{m,fid}^b(f(\mathbf{x}), b(\mathbf{x})), \tag{23}$$

where $\mathbf{C}_m^f$ and $\mathbf{C}_m^b$ represent the control points computed at the current time step, and $\mathbf{C}_{m,0}^f$ and $\mathbf{C}_{m,0}^b$ are the control points defined at the initial transformation. ϵ_t is the time step which can be set using a line search algorithm. The displacement fields in the forward ($V_f(\mathbf{x})$) and backward ($V_b(\mathbf{x})$) directions are evaluated using Eqs. (10) and (11), respectively. In the second step, the computed displacement fields are regularized through the minimization of the energy functional $E_{reg}(V_f(\mathbf{x}), V_b(\mathbf{x}))$. We have

$$E_{reg}(V_f(\mathbf{x}), V_b(\mathbf{x})) = \lambda_1 \int_\Omega (\|\mathbf{x} + V_{f,u}(\mathbf{x})\|_2^2 + \|\mathbf{x} + V_{f,v}(\mathbf{x})\|_2^2 + \|\mathbf{x} + V_{f,w}(\mathbf{x})\|_2^2)\,d\Omega$$
$$+ \lambda_2 \int_\Omega (\|\mathbf{x} + V_{b,u}(\mathbf{x})\|_2^2 + \|\mathbf{x} + V_{b,v}(\mathbf{x})\|_2^2 + \|\mathbf{x} + V_{b,w}(\mathbf{x})\|_2^2)\,d\Omega$$
$$+ \lambda_3 \int_\Omega [(l_f(\mathbf{x}) \circ l_b(\mathbf{x}) - \mathbf{x})^2 + (l_b(\mathbf{x}) \circ l_f(\mathbf{x}) - \mathbf{x})^2]\,d\Omega, \tag{24}$$

where $l_f(\mathbf{x}) = \mathbf{x} + V_f(\mathbf{x})$ and $l_b(\mathbf{x}) = \mathbf{x} + V_b(\mathbf{x})$. Regularization of the transformation function is a crucial step in order to ensure smooth and realistic deformation of the image. There are three terms added for regularization in the optimization process. The first order regularization terms corresponding to λ_1 and λ_2 maintain smoothness in the deformations in each parametric direction [28–31]. We set $\lambda_1 = \lambda_2$ to maintain symmetry in the optimization. The bidirectional composition regularization term associated with λ_3 constrains the composition of the forward and backward transformations to be identity. This makes the framework more symmetric, which is desirable for reducing bias in medical image registration. The energy functional is minimized using the L^2 gradient flow method as shown in Eqs. (18) and (19). Thus the control points are updated as follows

$$\frac{\mathbf{P}_m^f - \mathbf{C}_m^f}{\epsilon_t} = -\delta E_{m,reg}^f(V_f(\mathbf{x}), V_b(\mathbf{x})), \tag{25}$$

$$\frac{\mathbf{P}_m^b - \mathbf{C}_m^b}{\epsilon_t} = -\delta E_{m,reg}^b(V_f(\mathbf{x}), V_b(\mathbf{x})), \tag{26}$$

where $\mathbf{C}_m^f$, $\mathbf{C}_m^b$ and $\mathbf{P}_m^f$, $\mathbf{P}_m^b$ are control points computed at the first and second step of the minimization respectively. The first order variation of the energy functional is given as

$$
\begin{aligned}
\delta E_{m,reg}^f(V_f(\mathbf{x}), V_b(\mathbf{x})) = {} & 2\lambda_1 \int_\Omega [V_{f,u}(\mathbf{x})B_{m,u}(\mathbf{x}) + V_{f,v}(\mathbf{x})B_{m,v}(\mathbf{x}) + V_{f,w}(\mathbf{x})B_{m,w}(\mathbf{x})]\,\mathrm{d}\Omega \\
& + 2\lambda_3 \int_\Omega (l_f(\mathbf{x}) \circ l_b(\mathbf{x}) - \mathbf{x})B_m(l_b(\mathbf{x}))\,\mathrm{d}\Omega \\
& + 2\lambda_3 \int_\Omega (l_b(\mathbf{x}) \circ l_f(\mathbf{x}) - \mathbf{x})D(l_b(l_f(\mathbf{x})))B_m(\mathbf{x})\,\mathrm{d}\Omega,
\end{aligned}
\tag{27}
$$

$$
\begin{aligned}
\delta E_{m,reg}^b(V_f(\mathbf{x}), V_b(\mathbf{x})) = {} & 2\lambda_2 \int_\Omega [V_{b,u}(\mathbf{x})B_{m,u}(\mathbf{x}) + V_{b,v}(\mathbf{x})B_{m,v}(\mathbf{x}) + V_{b,w}(\mathbf{x})B_{m,w}(\mathbf{x})]\,\mathrm{d}\Omega \\
& + 2\lambda_3 \int_\Omega (l_f(\mathbf{x}) \circ l_b(\mathbf{x}) - \mathbf{x})D(l_f(l_b(\mathbf{x})))B_m(\mathbf{x})\,\mathrm{d}\Omega \\
& + 2\lambda_3 \int_\Omega (l_b(\mathbf{x}) \circ l_f(\mathbf{x}) - \mathbf{x})B_m(l_f(\mathbf{x}))\,\mathrm{d}\Omega.
\end{aligned}
\tag{28}
$$

Here $D(l_b(l_f(\mathbf{x})))$ and $D(l_f(l_b(\mathbf{x})))$ are the Jacobian matrices with respect to $l_f(\mathbf{x})$ and $l_b(\mathbf{x})$ respectively. $B_{m,u}(\mathbf{x})$, $B_{m,v}(\mathbf{x})$ and $B_{m,w}(\mathbf{x})$ are the partial derivatives of the basis functions $B_m(\mathbf{x})$ with respect to u, v and w. The final displacement fields for both the forward and backward transformation functions are evaluated using Eqs. (10) and (11). The gradients of $I_s(\mathbf{x})$ and $I_t(\mathbf{x})$ and the level set contour $\phi(\mathbf{x})$ are computed by evaluating the derivatives of the B-spline kernel. Thus we can obtain smooth deformation field and smooth geometric representation of the segmentation result simultaneously, unlike finite difference based algorithms. The level set contours represent the geometry more accurately.

2.3. Adaptive refinement using THB-splines

Local refinement plays an important role in improving the efficiency of the joint framework. Due to the tensor product nature of B-splines, it is difficult to perform local and adaptive refinement. Therefore, several methods such as T-splines [32], hierarchical B-splines [33], LR-splines [34] and PHT-splines [35] were proposed by modifying the basis functions to support local refinement. As compared to PHT-splines, HB-splines and THB-splines are a better choice for the image registration framework because they allow for more general refinements. It is preferable to work with hierarchical splines due to the ease of construction. In addition, PHT-splines have reduced continuity as compared to THB-splines of the same polynomial order. This results in higher number of degrees of freedom for the same level of accuracy.

Hierarchical B-splines (HB-splines) have been shown to improve the efficiency of image registration algorithms [28,30, 36]. In HB-splines, the regions of interest are locally refined by introducing hierarchy of tensor-product B-splines defined at multiple refinement levels. These basis functions are non-negative and linearly independent. We explain the construction of HB-splines for univariate splines (see Fig. 1). The tensor product nature of HB-splines allows a simple extension to higher dimensions. Consider the univariate cubic B-splines, $B^{0,3}(u)$, defined over the domain $u \in \Omega_0 = [0, 10]$. The knot vector is given as $U = 0, 1, \ldots, 10$. Each B-spline $B_i^{0,3}(u)$ in this parametric domain has local support defined as $\text{supp}(B_i^{0,3}(u)) = [u_i, u_{i+p+1}]$, where $p = 3$ is the degree of the B-spline basis function. The B-spline basis function (the red curve) is replaced by its five children basis functions (the green curves in Fig. 1(c)) at the next refinement level (Ω_1), where the knot vector is obtained by bisecting the knot vector of the previous refinement level. In general, any father basis function at the refinement level l can be represented as the linear combination of its children B-splines at refinement level $l + 1$, which are set as active. Such refinability property gives

$$B_i^{l,3}(u) = \sum_{j=1}^{N_c} c_{i,j} B_j^{(l+1),3}(u), \tag{29}$$
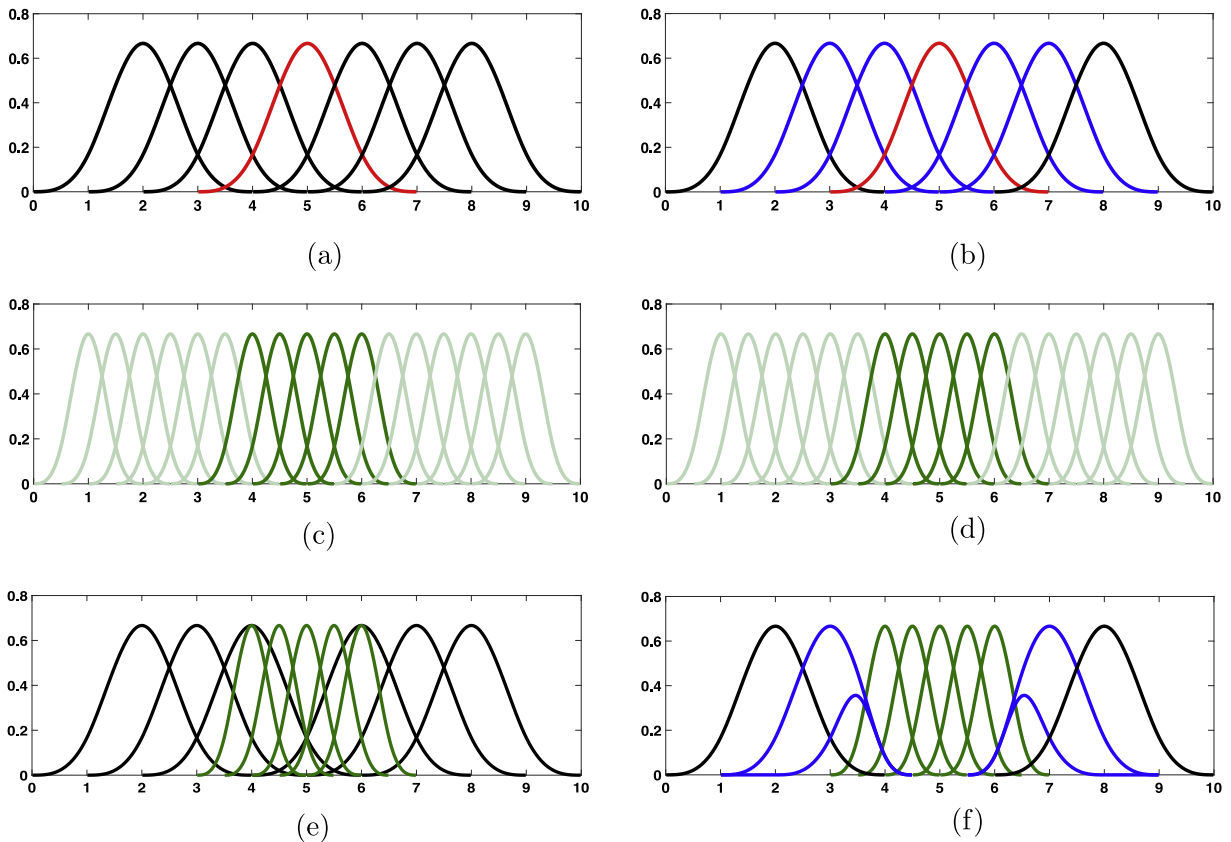
Fig. 1. Schematic representation of the construction of HB-splines versus THB-splines. First column: B-splines at coarser level (a), B-splines at finer level, the children B-splines are shown in dark green color (c), collecting active splines from both the levels to construct HB-splines (e). Second column: B-splines at coarser level, truncated B-splines are shown in blue color (b), B-splines at finer level, the children B-splines are shown in dark green color (d), collecting active splines from both the levels to construct THB-splines (f). The active splines are shown in black, dark green and blue colors. The inactive splines are shown in red color.

where $c_{i,j}$ are the subdivision coefficients determined using the knot insertion algorithm and N_c is the number of children B-splines. By performing the two-step refinement of HB-splines recursively, the refinement can be extended to multiple levels. Although HB-splines provide an efficient implementation of local refinement, there are certain drawbacks associated with the basis functions. In particular, the basis functions have more overlap, which subsequently increases with the number of refinement levels. In addition, the partition of unity property is not satisfied. THB-splines [37] are an improvement over HB-splines, in which they preserve all the useful properties but in addition have reduced overlap between basis functions at different levels and form a partition of unity. As can be seen in Fig. 1(b), in addition to the inactive basis function (the red curve), the basis functions with partial support in Ω_1 are truncated (the blue curves). The refinability equation (given in Eq. (29)) for the truncated basis functions is modified as

$$B_i^{l,3}(u) = \sum_{j=1, \, supp(B_j^{(l+1),3}(u)) \notin \Omega_1}^{N_c} c_{i,j} B_j^{(l+1),3}(u), \tag{30}$$

by removing the support of the children B-splines already set as active in Ω_1. The construction of THB-splines involves the assembly of active basis functions at the levels l and $l+1$:

$$B^{l,3}(u) \cup B^{(l+1),3}(u). \tag{31}$$

In the proposed method, we demonstrate adaptive local refinement using THB-splines in a multiresolution framework as shown in Algorithm 1. We perform the joint framework on images by first constructing an image pyramid. For each image resolution, adaptive refinement is carried out. The spatial transformation computed at a lower image resolution is projected to the next level. In this way, we can improve the computational efficiency. Instead of performing the joint segmentation and registration at one image resolution, we split up the computation by first computing the coarser deformation at the lower image resolution and finer deformation at the higher image resolution.

2.4. Software implementation

We have developed an open source software package in MATLAB 2018a environment with all the examples included in the article for reference at the link: (https://github.com/arpawar/JISR). In this package, we have divided the code into separate modules to make it easier for the user to modify. The parameters $\theta_1, \theta_2, \rho, \epsilon, \lambda_1, \lambda_2, \lambda_3$, the number of elements at the first level, the maximum number of levels and the maximum number of iterations can be set in the *setparameters.m* file. Most examples can be run on a computer with 2.5 GHz quad-core Intel Core i7 processor and 16 GB RAM.

Since we perform a bidirectional composite update using B-splines, the computation can become expensive. We have introduced parallel computation in the subroutines where the computations are intensive. We use the Parallel Computing Toolbox in MATLAB, specifically the parfor loops to increase the computation speed. Moreover, the functions that are computationally expensive can be converted into C++ functions using MEX functions. Utilizing C++ functions increases the code efficiency. The parfor loops in the MEX functions are further converted to OpenMP to utilize multiple cores to carry out the computation. For 3D images with larger sizes, the results have been computed on the supercomputers at Extreme Science and Engineering Discovery Environment (XSEDE) supercomputer called Bridges [38] in Pittsburgh Supercomputer Center. Here the software was run on a node with 28 cores having RAM capacity of 128 GB.

Algorithm 1: Description of the joint framework with local refinement using THB-splines

---

Input : Source (atlas) image $I_s(\mathbf{x})$, segmented atlas image $\phi(\mathbf{x})$ and target image $I_t(\mathbf{x})$ of resolution N. $\mathbf{C}_0^f$ and $\mathbf{C}_0^b$ are the initialized B-spline control points for the forward and backward displacement fields such that $V_f(\mathbf{x}) = \mathbf{0}$ and $V_b(\mathbf{x}) = \mathbf{0}$. $f(\mathbf{x}) = \mathbf{x}$ and $b(\mathbf{x}) = \mathbf{x}$.

Output: $f(\mathbf{x})$ and $b(\mathbf{x})$ such that $I_s(f(\mathbf{x})) \approx I_t(\mathbf{x})$, $\phi(f(\mathbf{x}))$ represents segmented target image and $I_t(b(\mathbf{x})) \approx I_s(\mathbf{x})$.

 1: **for** level $l = 1$ to l_max **do**
 2: Scale $I_s^l(f(\mathbf{x}))$, $\phi^l(f(\mathbf{x}))$ and $I_t^l(b(\mathbf{x}))$ to the resolution $\frac{N}{2^{lmax-l}}$
 3: **if** $l > 1$ **then**
 4:   Compute $I_g = |\nabla(I_s^{l-1}(f(\mathbf{x})) - I_t(\mathbf{x}))|$ at the centroids of the elements of the control grid, where $I_s^{l-1}(f(\mathbf{x}))$ is the evolving image obtained at the end of the previous refinement level. Evaluate $G_{mean} = \text{mean}(I_g)$.
 5:   **for** all the active B-splines $B^{THB}(\mathbf{x})$ at $level = l - 1$ **do**
 6:    Compute G_j which is the average I_g value for elements within the support of each active B-spline $B_j^{THB}(\mathbf{x})$
 7:    **if** $G_j > \rho G_{mean}$ **then**
 8:     REFINE $B_j^{THB}(\mathbf{x})$
 9:    **end if**
10:   **end for**
11: **end if**
12: Assemble active basis functions to obtain hierarchical structure. Set the iteration counter $i = 0$.
13: While $DS(i + 1) - DS(i) > \Delta$ OR $i < \text{MAXITER}$:

  1. STEP 1: Evaluate the new positions of the control points for both the forward and backward displacement fields $\mathbf{C}^{f,l}$ and $\mathbf{C}^{b,l}$ using Eqs. (22)-(23).
  2. Compute the displacement field for the first step $V_f(\mathbf{x})$ and $V_b(\mathbf{x})$ using Eqs. (10)-(11).
  3. STEP 2: Update the active control points $\mathbf{P}^{f,l}$ and $\mathbf{P}^{b,l}$ using the control points $\mathbf{C}^{f,l}$ and $\mathbf{C}^{b,l}$ as given in Eqs. (25)-(26). Using $\mathbf{P}^{f,l}$ and $\mathbf{P}^{b,l}$, compute the displacement field for the second step $V_f(\mathbf{x})$ and $V_b(\mathbf{x})$ using Eqs. (10)-(11).
  4. Compute the spatial transformation function: $f_{i+1}(\mathbf{x}) = f_i(\mathbf{x}) \circ (\mathbf{x} + V_f(\mathbf{x}))$. Similarly, in the backward direction, $b_{i+1}(\mathbf{x}) = b_i(\mathbf{x}) \circ (\mathbf{x} + V_b(\mathbf{x}))$. Compute the evolving images $I_s^l(f(\mathbf{x}))$, $I_t^l(b(\mathbf{x}))$ and the level set function defining the segmentation contour $\phi^l(f(\mathbf{x}))$.
  5. $i = i + 1$

14: Scale the images $I_s^l(f(\mathbf{x}))$, $\phi^l(f(\mathbf{x}))$ and $I_t^l(f(\mathbf{x}))$ to full image resolution.
15: **end for**

---

3. Numerical results and discussion

In this section, we evaluate the performance of our proposed joint segmentation and registration algorithm on synthetic and medical images. The comparison of the accuracy is shown for our method along with other segmentation [39] and registration methods [14,28]. Since we apply our joint framework on grayscale images with the same range of intensity, we use Mean Squared Difference (MSD) as a similarity metric to correlate the images and quantify the registration error. For a pair of grayscale images I_s and I_t with the total number of pixels as N, MSD is defined as

$$MSD = \frac{\sum_{i=1}^{N} (I_s(i) - I_t(i))^2}{N}. \tag{32}$$

MSD gives a good estimation of the average error between the registered and the target image, where a smaller value corresponds to a better match between images. To assess the segmentation accuracy we use the Dice Similarity (DS)

Table 1
Parameter values for the examples shown.

Images	θ_1	θ_2	λ_1	λ_2	λ_3	ρ (levels: 2, 3)	ϵ (levels: 1, 2, 3)
C-shape (Fig. 2)	100	1	0.01	0.01	0.01	(0.50, 1.00)	(0.40, 0.40, 0.40)
Triangle (Fig. 3)	100	1	0.10	0.10	0.01	(0.05, 0.10)	(0.35, 0.35, 0.35)
Brain MRI (Fig. 5)	0.5	2	0.01	0.01	0.01	(0.20, 0.50)	(0.50, 0.50, 0.50)
Lung CT (Fig. 6)	1	2	0.01	0.01	0.01	(0.50, 1.00)	(0.10, 0.10, 0.20)
Bunny image (Fig. 7)	50	1	0.10	0.10	0.01	(0.50, 1.00)	(0.20, 0.15, 0.08)
Brain MRI (Fig. 8)	1	1	0.001	0.001	0.001	(0.50, 3.50)	(0.20, 0.15, 0.08)

Table 2
Comparison of the MSD and DS metrics of the level set method, the DTHB_2D method and our joint segmentation and registration method.

Images	MSD			DS		
	Level set	DTHB_2D	Joint S-R	Level set	DTHB_2D	Joint S-R
C-shape (Fig. 2)	4.9×10^{-3}	7.4×10^{-3}	3.1×10^{-3}	98.28%	96.98%	98.81%
Triangle (Fig. 3)	5.1×10^{-3}	7.6×10^{-3}	1.1×10^{-3}	98.11%	95.56%	99.58%
Brain MRI (Fig. 5)	3.9×10^{-3}	8.4×10^{-3}	2.8×10^{-3}	91.54%	86.05%	93.14%
Lung CT (Fig. 6)	5.7×10^{-4}	3.10×10^{-3}	5.4×10^{-4}	93.89%	92.67%	94.63%

metric which evaluates the spatial overlap of the different labeled regions of the segmented image with the ground truth image. The DS metric for a particular class label denoting the region of interest is defined as

$$DS(label) = \frac{2N_c}{N_r + N_t} \times 100\%, \tag{33}$$

where N_c, N_r and N_t are the number of voxels identified as a particular label for the regions common to both the registered and target images, the registered images and the target images, respectively. As the value of DS approaches 100%, the segmentation result is closer to the ground truth image. During segmentation, the image is partitioned into several regions and assigned the class labels. This coefficient gives a good quantitative estimation of the overlap of the regions identified in the segmented image with the ground truth.

Initial discretization influences the convergence of the solution during the optimization process. Using a very coarse initial grid can speed the optimization but can sometimes lead to divergence and unrealistic deformations. By observing the convergence of the solution and the final accuracy, we can choose an optimal size of the initial grid. We use the same number of elements for the initial grid for the synthetic and medical images. This makes the method more general, requiring fewer manual adjustments. Sometimes due to the increased complexity of the medical images, a finer initial grid is chosen in order to get better accuracy.

3.1. 2D images

In Figs. 2–6, we demonstrate the implementation of the joint framework for 2D synthetic and medical images. The parameters for each example are shown in Table 1. In order to improve efficiency, we implement the framework using a multiresolution scheme, where at each image resolution level we compute the spatial transformation function on the corresponding adaptive grids. For all the examples, we use three levels of resolution. The accuracy of the segmentation and registration is shown in Table 2, as compared to the level set method [14] and the dynamic 2D registration method using THB-splines (DTHB_2D) [28].

In Fig. 2 we perform a large deformation based registration of a circle to a C-shape. Note that the intensities of the images are normalized. The output of the joint algorithm is the registered image (Fig. 2(g)) with the final deformation mapping (Fig. 2(l, p)) and the segmentation result (Fig. 2(o)). The contour shows the demarcation of the boundaries of the image at the sign-change boundary. Through the comparison of results in Table 2, we can see that our algorithm outperforms other methods. Moreover, we show that we can capture smooth mapping for the forward and backward transformation functions simultaneously.

In Figs. 3–4, we demonstrate the robustness of our method towards capturing large deformation mappings between images that are corrupted with noise. We first show the application of the joint segmentation and registration framework of a circle to a triangle shape shown in Fig. 3. We carry out the joint method on three multiresolution levels. The evolving images obtained at the end of each image resolution are shown. We can see that our method shows the highest DS metric value and the lowest MSD value as compared to other methods. Next, we evaluate the robustness of our method to perform segmentation of images corrupted with noise as shown in Fig. 4. The four target images have the noise intensities 0.02, 0.05, 0.1 and 0.15. The comparison of the DS metric of segmentation result obtained by our joint approach and the level set segmentation [39] is shown in Table 3. We can see from Fig. 4 that the segmented images contain no noise and have accurately segmented boundaries in comparison to performing image segmentation alone.
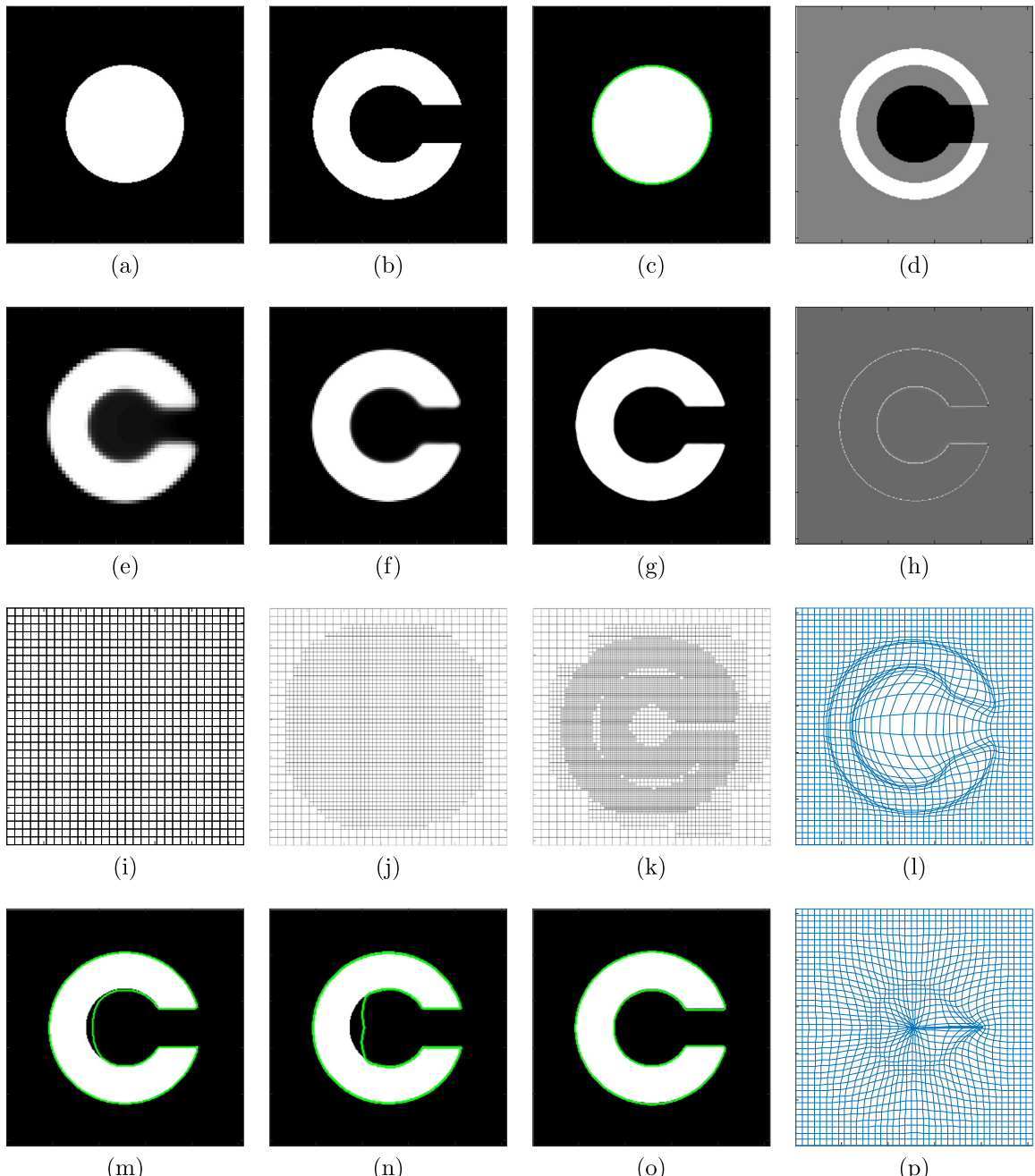
Fig. 2. Registration of circle to white C: the initial source image, the target image, the segmented source image and the initial image difference are shown in (a–d). The registered images obtained at each image resolution and the final image difference are shown in (e–h). The adaptively refined levels of B-splines at each image resolution level are shown in (i–k). The final level set contours overlaying the target images computed by the level set method, DTHB_2D and the joint framework are shown in (m–o). The forward and backward deformation grids are shown in (l) and (p).

DS metric for the segmentation result obtained through our joint approach is consistently higher than the image obtained from the level set segmentation method.

Unlike synthetic images, the segmentation and registration of medical images is more difficult to evaluate because they contain more detailed and complex physiological features. In Fig. 5 we study the application of the joint segmentation and registration framework for a brain MRI image [40]. The atlas image consists of the correctly labeled white matter region (see Fig. 5(c)), which is the input for the joint framework along with its corresponding MRI image (Fig. 5(a)). We evaluate the result on three image resolutions. At each image resolution an adaptive THB-spline grid is constructed. The regions of
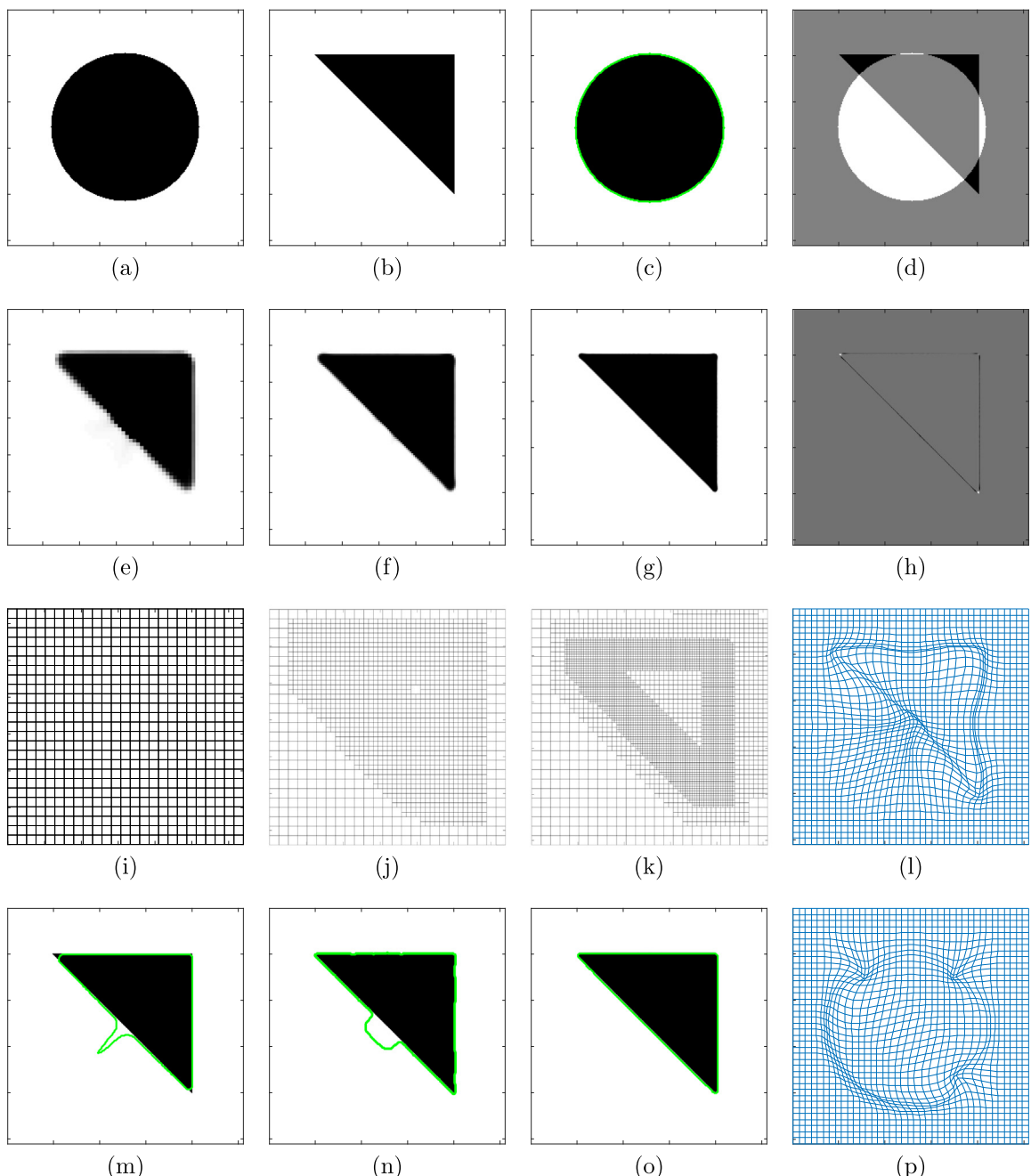
Fig. 3. Registration of circle to triangle: the initial source image, the target image, the segmented source image and the initial image difference are shown in (a–d). The registered images obtained at each image resolution and the final image difference are shown in (e–h). The adaptively refined levels of B-splines at each image resolution level are shown in (i–k). The final segmentation result by the level set method, DTHB_2D and the joint framework are shown in (m–o). The forward and backward deformation grids are shown in (l) and (p).

errors are identified and locally refined to capture finer details. The final segmented white matter of the target image (see Fig. 5(b)) is shown in Fig. 5(l). Certain concave and thin regions of the white matter are accurately captured in our result. This is largely due to the capturing of finer features by the fine splines in the adaptive grids. As seen from Table 2, we obtain a higher accuracy of both the segmentation and registration results. By introducing smooth representation of the evolving image and the level set function ϕ, there is intrinsic smoothness in the resultant images. We also demonstrate that we can obtain smooth and realistic forward and backward transformation functions as can be seen in Fig. 5(m, n).
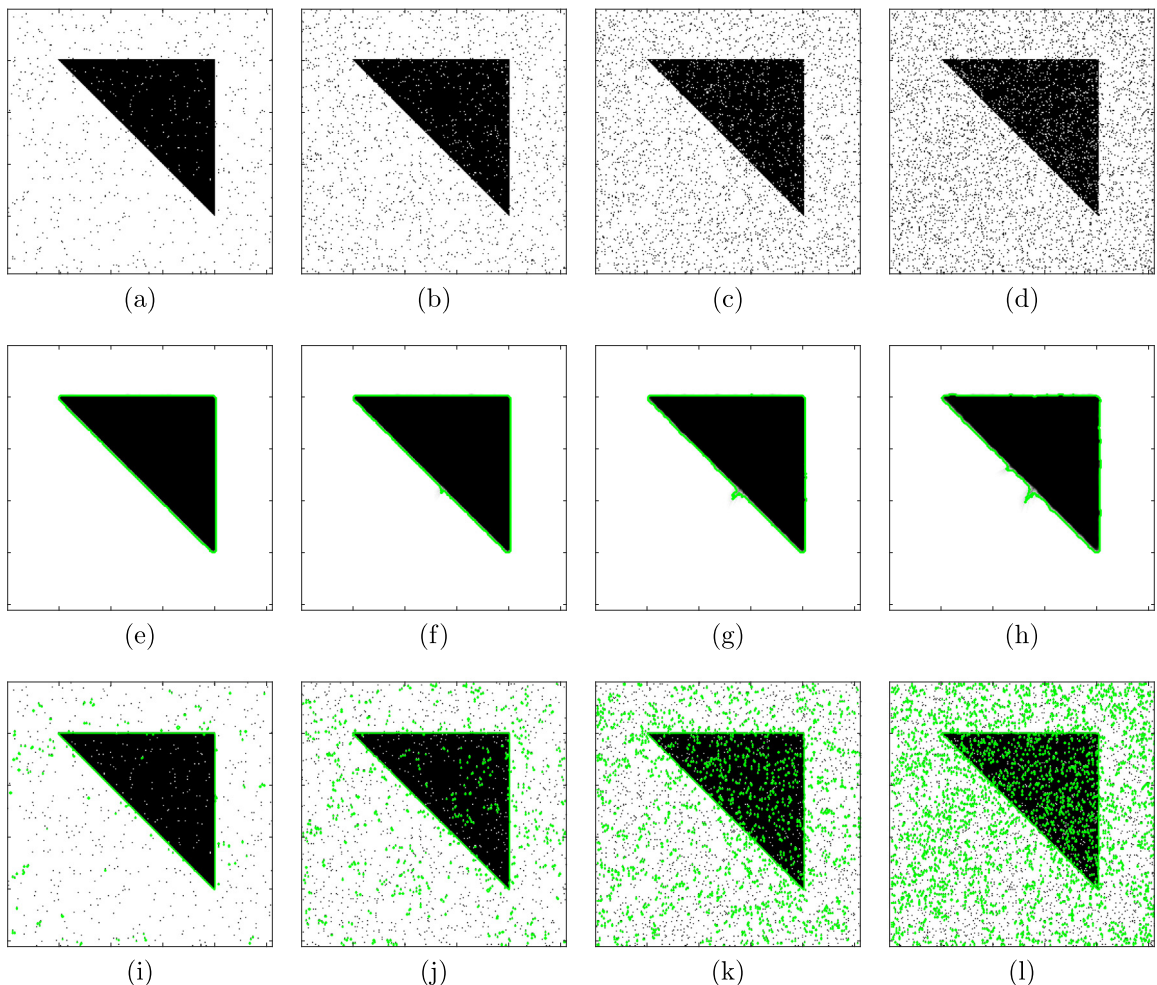
Fig. 4. Registration of circle in Fig. 3(a) to triangle: the target image with noise intensities 0.02, 0.05, 0.1 and 0.15 (a–d). The corresponding registered images with the segmentation contours (free of noise) using our joint approach are shown in (e–h). The segmentation results obtained for the corresponding noise intensities using the level set segmentation method [39] are shown in (i–l) where the segmented contours are noisy.

Table 3
The DS metric of the triangle image with different noise intensities for the level set segmentation method [39] and our joint framework.

Noise intensity	Level set segmentation	Joint S-R
0.02	99.32%	99.41%
0.05	96.76%	99.34%
0.10	91.83%	99.08%
0.15	85.39%	98.96%

In Fig. 6 we study the joint image segmentation and registration for lung images [41]. We evaluate the non-rigid registration of lungs during a breathing cycle. The source and target images are taken from the inhale and exhale stages, respectively. We evaluate the segmentation contour for the source image using the level set segmentation method. The evolving images are shown for each resolution level in Fig. 6(e–g). We can see that we get higher accuracy and at the same time capture the smooth deformation in order to correctly align the images. The final segmentation result correctly classifies the boundary of the lung for exhale stage in the target image. Local refinement is carried out near the lung boundaries, thus enabling the capture of finer scale deformations to correctly compute the deformation of the lung boundaries during the breathing cycle.
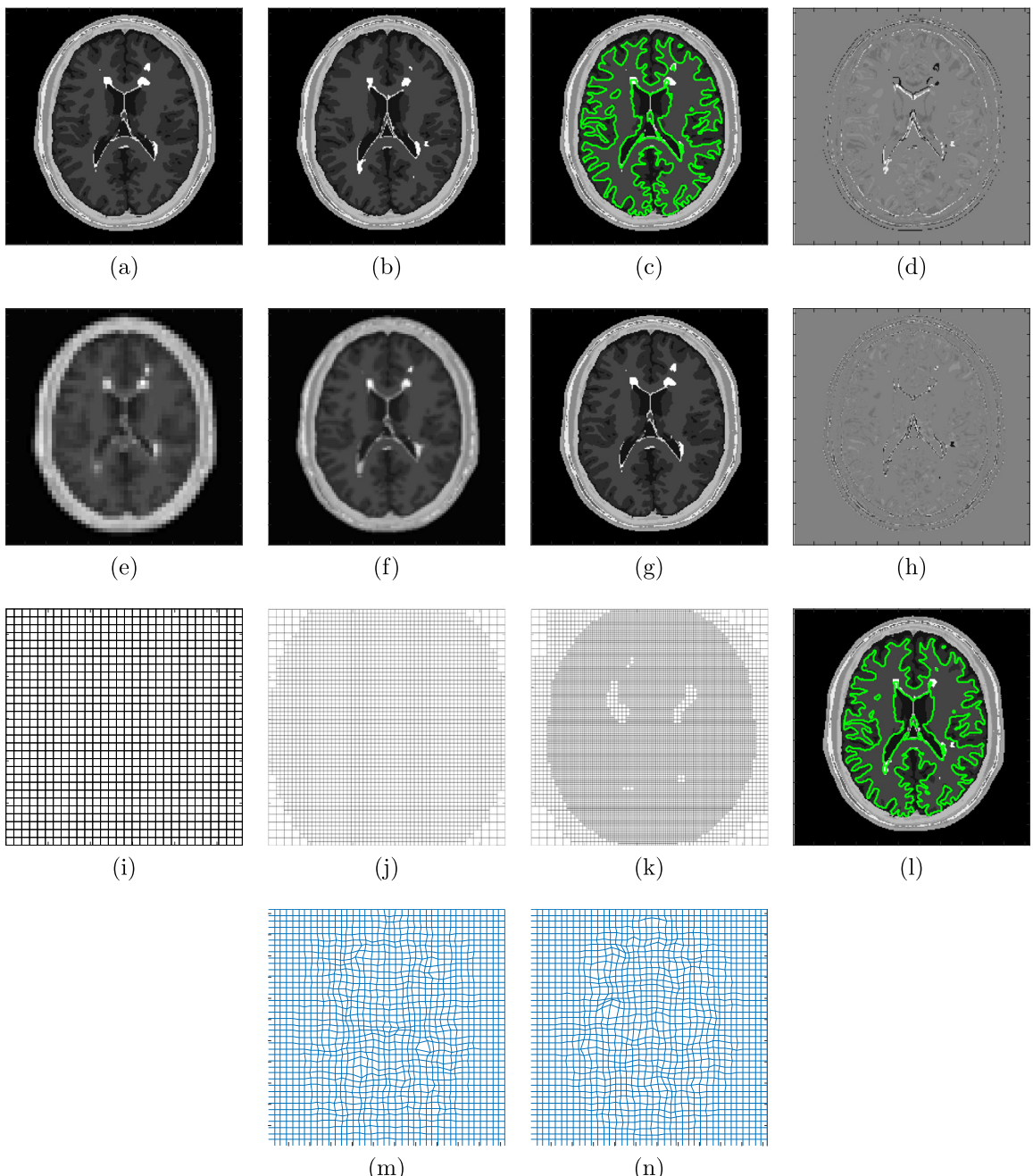
Fig. 5. Registration of brain atlas images: the initial source image, the target image, the segmented source image and the initial image difference are shown in (a–d). The registered images obtained at each image resolution and the final image difference are shown in (e–h). The adaptively refined levels of B-splines and the final segmentation result are shown in (i–l). The forward and backward deformation grids are shown in (m) and (n).

3.2. 3D Images

The joint image segmentation and registration method proposed in [23,24] computes accurate segmentation result by imposing hyperelasticity constraints to capture the complex deformations. However it can become computationally very expensive when extended for 3D images and is thus limited to 2D images only. Since we use free-form deformation with B-splines to capture the complex deformations, our approach can be easily extended to 3D. In Fig. 7 the joint approach is implemented to compute the large deformation of the sphere to a bunny image. This is a classic example for a large deformation study, where there are some sharp and concave features present in the target image (near the ears of the
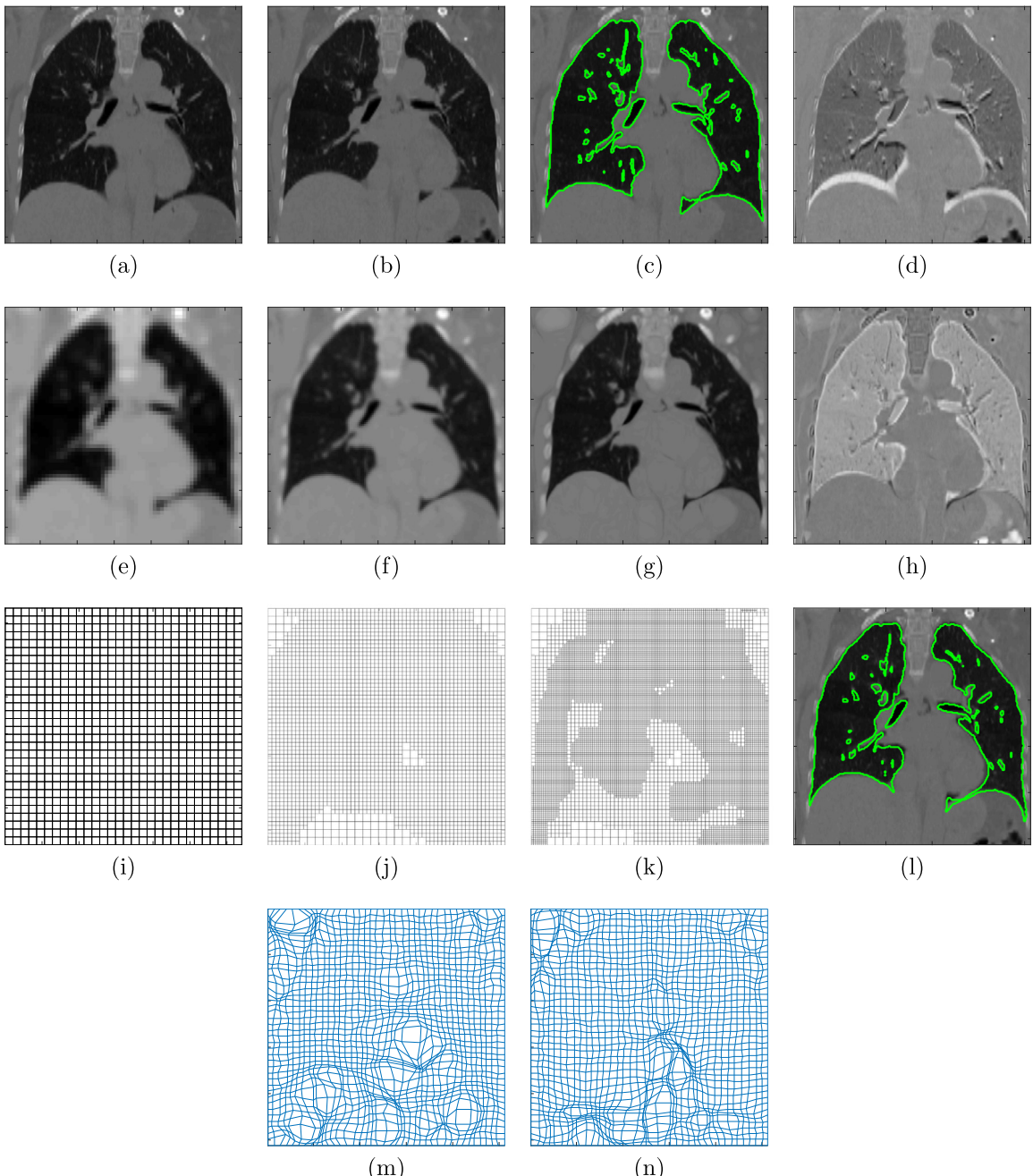
Fig. 6. Registration of lung images: the initial source image, the target image, the segmented source image and the initial image difference are shown in (a–d). The registered images obtained at each image resolution and the final image difference are shown in (e–h). The adaptively refined levels of B-splines and the final segmentation result are shown in (i–l). The forward and backward deformation grids are shown in (m) and (n).

inary image, the demarcation of the boundary is very clear. Thus the parameter associated with segmentation (θ_1) is set to a higher value than the parameter associated with the registration (θ_2). We evaluate the three image resolution levels. At each step we compute the solution on adaptive grids fitted to the image resolution. The initial grid size is set as $20 \times 20 \times 20$. The proposed algorithm correctly captures the boundaries of the highly complex shape of the bunny model as compared to the level set method. As seen from the registration result in Fig. 7(e), the algorithm can accurately capture the concave and thin structures that are present in the image. The DS metric for the image is 98.86%. In comparison, the DS metric for the segmented images obtained using the level set [14]
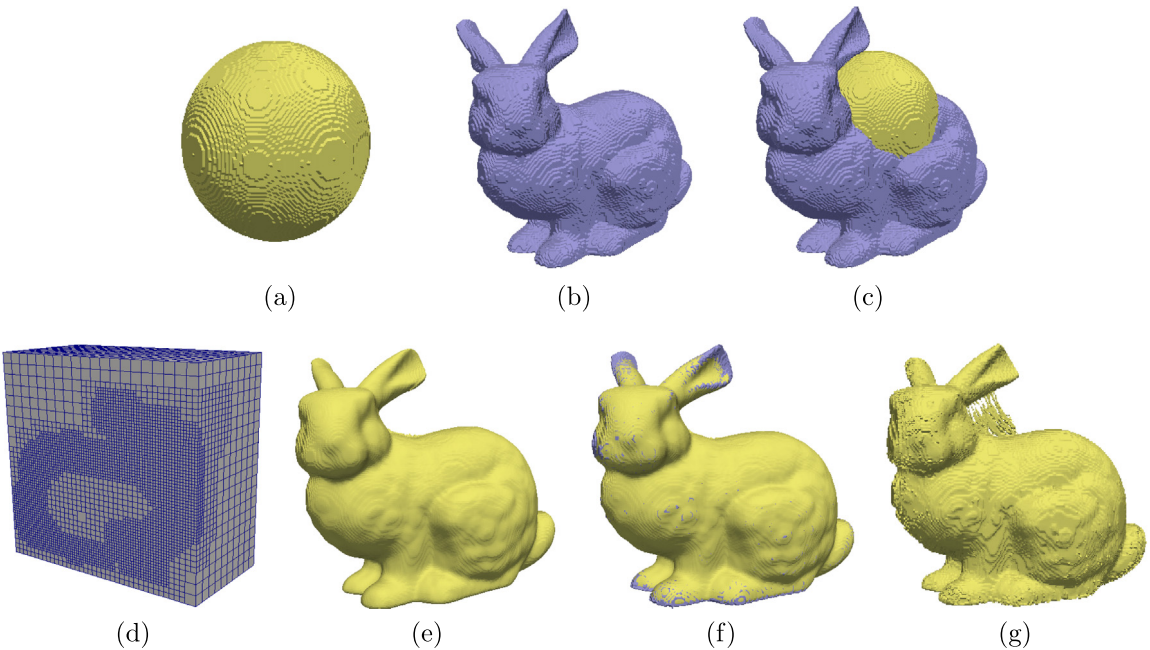
Fig. 7. Registration of sphere to bunny: the initial source image, the target image and the initial image difference are shown in (a–c). The adaptively refined grid of THB-splines obtained at the maximum refinement level, the registered images obtained by our joint S-R method, the final image difference and the registered image using the level set method [14] are shown in (d–g).

and DTHB3D_Reg [28] methods are 98.68% and 95.96%, respectively. This example perfectly exemplifies the robustness of our method as compared to other approaches.

As shown in Fig. 8, we conduct an experiment for the joint segmentation and registration of brain MRI images taken from Brainweb database [40]. Here we use 10 pairs of images to perform the evaluation of the accuracy. The ground truth segmentation of gray matter is used as the input for the framework. Adaptive refinement is carried out for three multiresolution levels. Due to the larger size of images and the increased complexity of the physiological features represented by the MRI scans, it can be challenging to efficiently perform the joint algorithm. The goal is to increase the accuracy while at the same time not increase the computational effort. Here adaptive refinement is crucial to improve the efficiency of our algorithm, as the algorithm automatically adds control points in regions where finer details need to be captured. This saves a lot of computational time while maintaining high accuracy.

In order to measure the accuracy of the registered images by our method, we evaluate the DS metric for 10 pairs of images for different regions of the brain anatomy as shown in Fig. 9. We compute the DS metric for 12 materials of the brain MRI images. The DS metric for these labels is compared with the level set method [14] and the DTHB3D_Reg method [28]. Here we can see that for most of the materials, we can get similar or higher accuracy for image segmentation. Since we used the ground truth segmentation of the gray matter as the input, our approach shows slightly higher DS metric for the same, 82.60% vs. 82.29% (the level set method) and 78.93% (the DTHB3D_Reg method).

Different from our previous work [28,30], in this paper we develop a joint segmentation and registration framework to improve the registration accuracy. Since in this framework both registration and segmentation are carried out, the computational cost is larger than our previous registration framework. Unlike our previous approach, where the spatial transformation function is evaluated at the full image resolution, we adopt a multiresolution framework where local refinement of B-splines is carried out on an image pyramid. This improves the efficiency and robustness of the computation. To improve the accuracy as compared to [28,30], we introduce smooth image representation and bidirectional registration. Finally, we implement composition update in order to capture large deformation more accurately as compared to the additive update used in [28,30].

4. Conclusions and future work

A joint variational level set framework based on THB-splines is proposed where image segmentation and registration are simultaneously carried out. We represent the level set function defining the segmentation result and the spatial transformation mapping using B-splines. In addition, a bidirectional composition update for the deformation field is introduced to ensure smoothness and increase symmetry in the transformation mapping. We show an improvement in the accuracy for both segmentation and registration of 2D and 3D images. All the source code of our software is available in the public domain (https://github.com/arpawar/JISR).
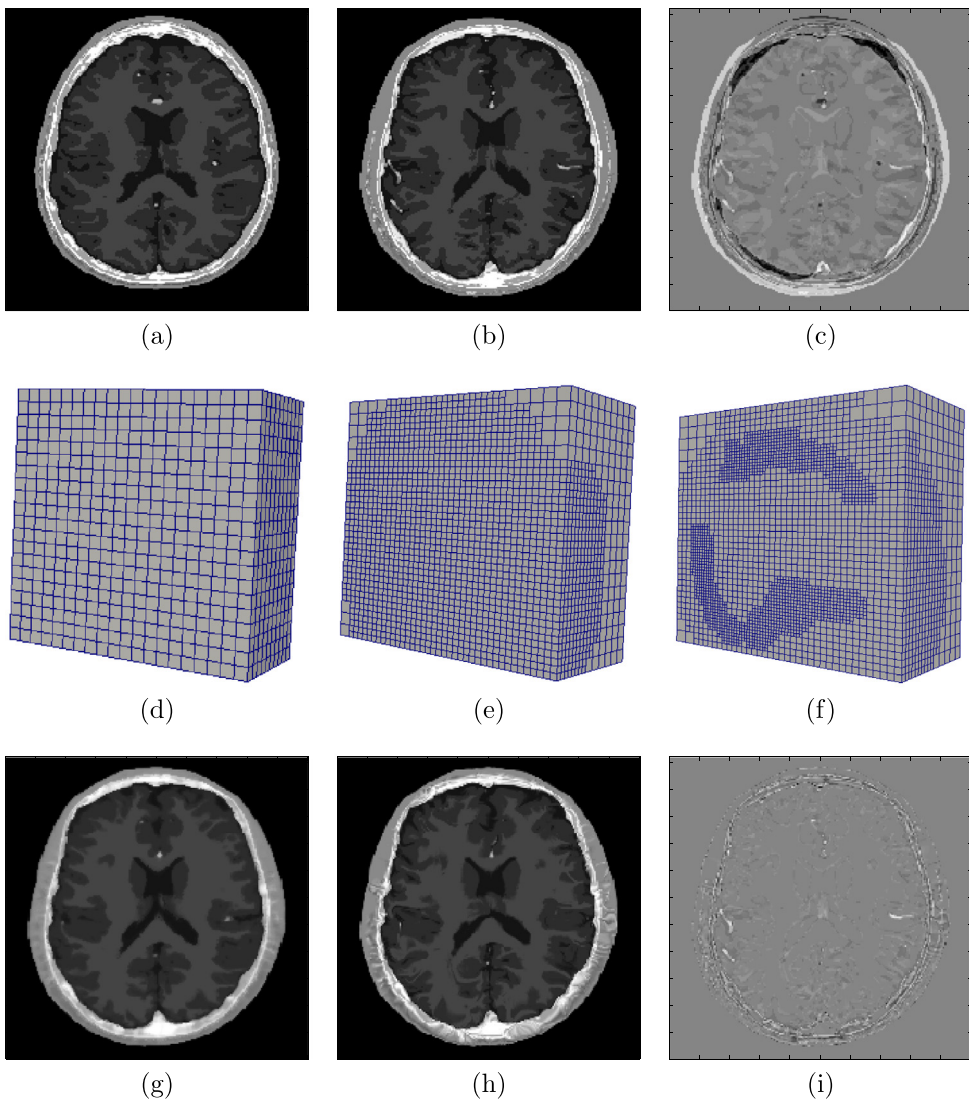
Fig. 8. Inter-patient registration of brain MRI images: the axial slice of the initial source image, the target image and the initial image difference are shown in (a–c). The adaptively refined THB-spline grids at the three refinement levels are shown in (d–f). The final registered images obtained using the level set method and our joint S-R method are shown in (g–h). The final image difference is shown in (i).
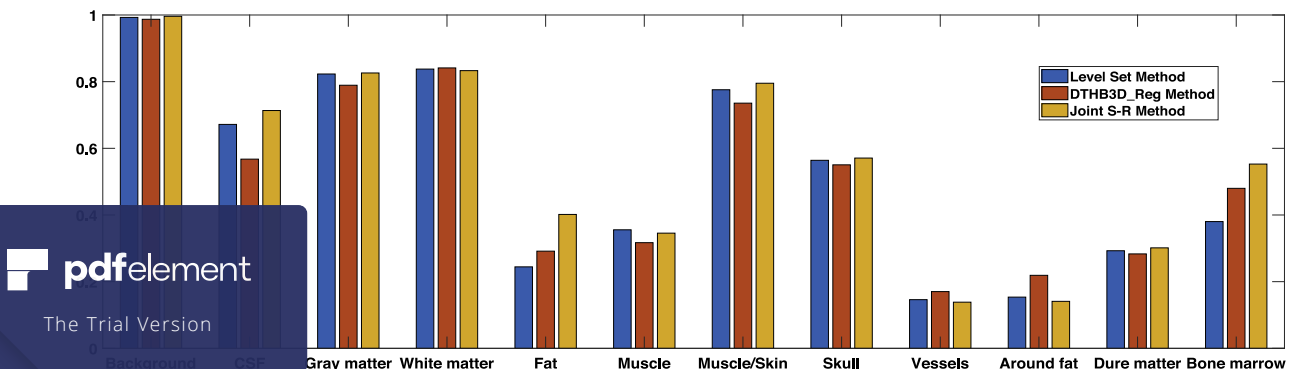

Fig. 9. Average segmentation accuracy between the registered images and the target images of 10 pairs of brain MRI evaluated using the level set method, the DTHB3D_Reg method and our joint segmentation and registration method, respectively.

In our future work, we will apply our joint segmentation and registration technique to patient-specific modeling from medical images. From an atlas image with expert aided segmentation result, a template geometry is created. By computing the physical deformation from the template to a patient-specific image, we can directly morph the template geometry to obtain patient-specific models. In the long run, these computational models will help medical professionals achieve a faster and better understanding of certain diseases, with more individualized treatments. In the current work, we use the Chan–Vese model [25] to perform the binary segmentation in the joint framework. We plan to extend this to perform multi-phase image segmentation with intensity heterogeneity [42]. We also plan to study the role of different local refinement techniques such as *p*-refinement and *hp*-refinement using B-splines in order to generalize and extend our joint framework.

Acknowledgments

References

[1] L.G. Brown, A survey of image registration techniques, ACM Comput. Surv. 24 (4) (1992) 325–376.

[2] B. Zitova, J. Flusser, Image registration methods: a survey, Image Vis. Comput. 21 (11) (2003) 977–1000.

[3] Y. Zhang, Y. Jing, X. Liang, G. Xu, L. Dong, Dynamic lung modeling and tumor tracking using deformable image registration and geometric smoothing, Mol. Cell. Biomech. 9 (3) (2012) 213–226.

[4] J.P. Pluim, J. Maintz, M.A. Viergever, Image registration by maximization of combined mutual information and gradient information, in: International Conference on Medical Image Computing and Computer-Assisted Intervention, Springer, 2000, pp. 452–461.

[5] K.S. Fu, J.K. Mui, A survey on image segmentation, Pattern Recognit. 13 (1) (1981) 3–16.

[6] F.P. Oliveira, J.M.R. Tavares, Medical image registration: a review, Computer Methods in Biomechanics and Biomedical engineering 17 (2) (2014) 73–93.

[7] A. Sotiras, C. Davatzikos, N. Paragios, Deformable medical image registration: a survey, IEEE Trans. Med. Imaging 32 (7) (2013) 1153–1190.

[8] T. Vercauteren, X. Pennec, A. Perchant, N. Ayache, Diffeomorphic demons: efficient non-parametric image registration, NeuroImage 45 (1) (2009) S61–S72.

[9] B.B. Avants, C.L. Epstein, M. Grossman, J.C. Gee, Symmetric diffeomorphic image registration with cross-correlation: evaluating automated labeling of elderly and neurodegenerative brain, Med. Image Anal. 12 (1) (2008) 26–41.

[10] J. Ashburner, A fast diffeomorphic image registration algorithm, NeuroImage 38 (1) (2007) 95–113.

[11] H. Lombaert, L. Grady, X. Pennec, N. Ayache, F. Cheriet, Spectral log-demons: diffeomorphic image registration with very large deformations, Int. J. Comput. Vis. 107 (3) (2014) 254–271.

[12] T. Vercauteren, X. Pennec, A. Perchant, N. Ayache, Non-parametric diffeomorphic image registration with the demons algorithm, in: International Conference on Medical Image Computing and Computer-Assisted Intervention, Springer, 2007, pp. 319–326.

[13] N.J. Tustison, B.B. Avants, Explicit B-spline regularization in diffeomorphic image registration, Front. Neuroinformatics 7 (2013) 39.

[14] C.L. Chan, C. Anitescu, Y. Zhang, T. Rabczuk, Two and three dimensional image registration based on B-spline composition and level sets, Commun. Comput. Phys. 21 (2) (2017) 600–622.

[15] S. Ying, D. Li, B. Xiao, Y. Peng, S. Du, M. Xu, Nonlinear image registration with bidirectional metric and reciprocal regularization, PLoS One 12 (2) (2017) e0172432.

[16] T.F. Chan, B. Sandberg, L.A. Vese, Active contours without edges for vector-valued images, J. Vis. Commun. Image Represent. 11 (2) (2000) 130–141.

[17] B. Vemuri, Y. Chen, Joint image registration and segmentation, Geom. Level Set Methods Imaging Vis. Graph. (2003) 251–269.

[18] S. Gorthi, V. Duay, X. Bresson, M.B. Cuadra, F.J.S. Castro, C. Pollo, A.S. Allal, J.P. Thiran, Active deformation fields: dense deformation field estimation for atlas-based segmentation using the active contour framework, Med. Image Anal. 15 (6) (2011) 787–800.

[19] T. Rohlfing, R. Brandt, R. Menzel, D.B. Russakoff, C.R. Maurer, Quo vadis, atlas-based segmentation?, in: Handbook of Biomedical Image Analysis, Springer, 2005, pp. 435–486.

[20] M. Droske, M. Rumpf, Multiscale joint segmentation and registration of image morphology, IEEE Trans. Pattern Anal. Mach. Intell. 29 (12) (2007) 2181–2194.

[21] P. Swierczynski, B.W. Papież, J.A. Schnabel, C. Macdonald, A level-set approach to joint image segmentation and registration with application to CT lung imaging, Comput. Med. Imaging Graph. 65 (2018) 58–68.

[22] C.V. Verhoosel, G.J. Van Zwieten, B. Van Rietbergen, R. de Borst, Image-based goal-oriented adaptive isogeometric analysis with application to the micro-mechanical modeling of trabecular bone, Comput. Methods Appl. Mech. Engrg. 284 (2015) 138–164.

[23] C.L. Guyader, L.A. Vese, A combined segmentation and registration framework with a nonlinear elasticity smoother, Comput. Vis. Image Underst. 115 (12) (2011) 1689–1709.

[24] N. Debroux, C.L. Guyader, A joint segmentation/registration model based on a nonlocal characterization of weighted total variation and nonlocal shape descriptors, SIAM J. Imaging Sci. 11 (2) (2018) 957–990.

[25] T. Chan, L. Vese, Active contours without edges, IEEE Trans. Image Process. 10 (2) (2001) 266–277.

[26] G. Farin, Curves and surfaces for computer-aided geometric design: a practical guide, Elsevier, 2014.

[27] G.E. Christensen, H.J. Johnson, Consistent image registration, IEEE Trans. Med. Imaging 20 (7) (2001) 568–582.

[28] A. Pawar, Y.J. Zhang, C. Anitescu, Y. Jia, T. Rabczuk, DTHB3D_Reg: dynamic truncated hierarchical B-spline based 3D nonrigid image registration, Commun. Comput. Phys. 23 (3) (2018) 877–898.

[29] Y. Jia, Y. Zhang, T. Rabczuk, A novel dynamic multilevel technique for image registration, Comput. Math. Appl. 69 (9) (2015) 909–925.

[30] A. Pawar, Y. Zhang, Y. Jia, X. Wei, T. Rabczuk, C.L. Chan, C. Anitescu, Adaptive FEM-based nonrigid image registration using truncated hierarchical B-splines, Comput. Math. Appl. 72 (8) (2016) 2028–2040.

[31] J. Leng, G. Xu, Y. Zhang, Medical image interpolation based on multi-resolution registration, Comput. Math. Appl. 66 (1) (2013) 1–18.
[32] T.W. Sederberg, J. Zheng, A. Bakenov, A. Nasri, T-splines and T-NURCCs, ACM Trans. Graph. (TOG) 22 (3) (2003) 477–484.
[33] D.R. Forsey, R.H. Bartels, Hierarchical B-spline refinement, ACM Siggraph Comput. Graph. 22 (4) (1988) 205–212.
[34] A. Bressan, Some properties of LR-splines, Comput. Aided Geom. Design 30 (8) (2013) 778–794.
[35] J. Deng, F. Chen, X. Li, C. Hu, W. Tong, Z. Yang, Y. Feng, Polynomial splines over hierarchical T-meshes, Graph. Models 70 (4) (2008) 76–86.
[36] Z. Xie, G.E. Farin, Image registration using hierarchical B-splines, IEEE Trans. Vis. Comput. Graphics 10 (1) (2004) 85–94.
[37] C. Giannelli, B. Jüttler, H. Speleers, THB-Splines: the truncated basis for hierarchical splines, Comput. Aided Geom. Design 29 (7) (2012) 485–498.
[38] J. Towns, T. Cockerill, M. Dahan, I. Foster, K. Gaither, A. Grimshaw, V. Hazlewood, S. Lathrop, D. Lifka, G.D. Peterson, XSEDE: accelerating scientific discovery, Comput. Sci. Eng. 16 (5) (2014) 62–74.
[39] C. Li, R. Huang, Z. Ding, J. Gatenby, D.N. Metaxas, J.C. Gore, et al., A level set method for image segmentation in the presence of intensity inhomogeneities with application to MRI, IEEE Trans. Image Process. 20 (7) (2011) 2007.
[40] BrainWeb: Simulated Brain Database, http://www.bic.mni.mcgill.ca/brainweb/.
[41] DIR-Lab: the deformable image registration laboratory, https://www.dir-lab.com/.
[42] C. Chen, J. Leng, G. Xu, A general framework of piecewise-polynomial Mumford–Shah model for image segmentation, Int. J. Comput. Math. 94 (10) (2017) 1981–1997.